# Interference effects of wind-over-top flow on high-rise buildings

Long Doan Sy*, Hitoshi Yamada, Hiroshi Katsuchi

*Department of Civil Engineering, Graduate School of Urban Innovation, Yokohama National University, Yokohama 2408501, Japan*

**Abstract**

Static and dynamic interference tests are performed by a series of wind tunnel tests to examine the existence and characteristics of wind-over-top (WOT) flow among high-rise buildings. A rigid-aerodynamic model or a principal model is a square cylinder with pressure taps and pivots on the elastic system. A value of pressure at each pressure tap and displacements at top of the principal model are measured for different wind velocities and directions. Two types of wooden rigid interference models in different heights with the principal model are put in different positions in the Cartesian axis. The experimental results showed that the WOT flow effects to a large area on the sides of the principal model in terms of the static pressures. A part of the front face of the principal model could increase by 46% mean pressure coefficient due to the presence of the WOT flow. Moreover, the WOT flow contribute the beneficial effects in term of dynamic structural design. In a close distance of two models, the WOT flow makes vortex-induced vibration of the principal model vibrate with small amplitude. In the larger distance, the WOT flow makes the principal model vibrate at high reduced velocity.

*Keywords:* Interference effect; wind-over-top flow; high-rise building

## 1. Introduction

There have been few detailed standards about wind-resistant design for high rise buildings due to mutual interference effects. Wind tunnel test is still an important method to design wind resistance in urban areas. This topic has become a concern for many researchers (Bailey & Kwok, 1985; Kim et al., 2009; Taniike, 1991, 1992; Xie & Gu, 2004; Yu & Xie, 2015; Zdravkovich, 1985) for decades. Other researches were concerned about a conical vortex on the rooftop (Banks & Meroney, 2001a, 2001b; Banks et al., 2000; Kawai, 2002; Marwood & Wood, 1997; Wu et al., 2001). The conical vortex produces a stationary negative pressure on the roof but does not move downward. The shear layer generated from the flat roof accompanies with the moving downward vortex on the side face, called Karman vortex, and forms the complex three-dimension type on the leeward path. This three-dimension (3-D) vortex is called an arch-type vortex (Kawai, 2002). A research on interference in details in this study will distinguish between effects from flows on the side and effects from the flow on the roof of a building called wind-over-top (WOT) flow.

An upstream building in interference tests, in general, reduces the mean response of the principal building by shielding effects. Due to various positions of the upstream building, some parts on cladding pressure or even the dynamic properties of the principal building turn into overestimated values (Yahyai et al., 1992). The peak oscillatory amplitude is likely to increase by three times in an interference test compared to isolated cases for both square and circular cylinders (Gowda & Kumar, 2006). The interference regime at a distance of x/B < 6 (B: width of the downstream model) is able to produce most of vortex shedding types (Zdravkovich, 1985). The sensitive height of the upstream building in interference tests is $0.5\text{-}1.5H_0$ ($H_0$: Height of the downstream building) (Kim et al., 2015; Xie & Gu, 2004). Therefore, the upstream building in double height to the height of the principal

46 building will remove all effects from flows on the roof of the upstream building.

47 In the isolated test, the combination of the WOT flow and Karman vortex turns into the arch-type
48 vortex which was initially mentioned in Kawai et al. (2009). This 3-D structure of wake is formed
49 just behind the square cylinder and always keeps its form during the formation and shedding of
50 Karman vortex. Although the tip of arch-type vortex stays still during the cycle of Karman vortex,
51 this type of vortex can stretch in the stream-wise direction (Kawai et al., 2012). In interference tests,
52 the principal building at downstream receives more angular momentum which is generated from the
53 shed vortices of an upstream building (Taniike, 1992). In addition, the presence of an upstream
54 building accelerates the flow and magnifies the pressure on the flat roof of a downstream building
55 (Pindado et al., 2011). However, the effects of only the WOT flow from the upstream building to the
56 downstream building in interference tests remain unclear.

57 Kim et al. (2015) indicated that the local pressure calculated by root-mean-square (RMS) near the
58 top of a building increases by up to 84% compared to an isolated building. The interference tests
59 with various positions show that the mean increase of mutual effects is only 13% to 40% on the
60 principal building (Hui et al., 2012; Xie & Gu, 2004; Yan & Li, 2016). The reason for high local
61 pressure on the side faces near the top is explained by the three-dimensional approaching flow
62 velocity and shear layer from the roof top of interference building. Therefore, the WOT flow from a
63 vicinity building plays an important contribution in the design of claddings on the side faces near the
64 top of the principal building.

65 To investigate the dynamic properties of a square cylinder, several methods have been applied by a
66 multiple-degree-of-freedom (MDOF) model or a single-degree-of-freedom (SDOF) model with
67 supporting systems at the base of models. A comparison of SDOF and MDOF models was conducted
68 by Yoshie et al. (1997) in a series of wind tunnel tests. The results showed that there is no significant
69 difference between SDOF and MDOF in across-wind of square cylinders. Moreover, the effect of the
70 motion-dependent force is more significant on the across-wind direction (Thanh et al., 2005).
71 Therefore, the research on the across-wind direction of a building is in demand.

72 This paper experimentally investigates the distribution of the WOT flow in high-rise buildings using
73 the wind tunnel tests in both static and dynamic phenomena. To examine the WOT flow, the
74 principal model with pressure taps is pivoted on the SDOF elastic system. This principal model is
75 located at the origin of the Cartesian coordinate system which is set-up on the wind tunnel floor. x-
76 axis is the along-wind direction, y-axis is the across-wind direction, and z-axis shows the height of
77 the model. Moreover, the reference models are wooden rigid models and locate at various positions
78 in xy-plane. Our main idea is to assess the characteristics of the WOT flow through tests of the same
79 height and double height interference models. The same height interference model produces the flow
80 which contains the WOT flow on the principal model. Meanwhile, the double height interference
81 model is high enough to ignore the effect of the WOT flow on the principal model. Comparisons of
82 the same height and double height interference tests in pressure coefficient and root-mean-square
83 (RMS) top displacement are expected to show the influence of the WOT flow. Particle image
84 velocimetry (PIV) measurement systems are also installed to analyze the WOT flow clearly.

85 **2. Rigid-aerodynamic-model system**

86 A rigid-aerodynamic-model system (Figure 1) was designed based on an idea of semi-rigid models
87 firstly represented by Balendra and Nathan (1987). The system was assembled by aluminum
88 materials. The natural frequency of structure possibly varied from 0.78 Hz – 10.58 Hz. The stiffness
89 was able to be modified by the mass of the model, the position of springs and spring stiffness. Oil
90 damping and damping cards were used to control the damping ratio of the model. Different oil
91 damping viscosities and sizes of damping cards gave different damping ratios to structures. The
92 vibration of the model could be measured by laser transducers through the moving of a damping card

93　under the wind tunnel floor or the moving of top of the model above the wind tunnel floor. With this
94　system, the instability vibration like vortex-induced vibration (VIV) or wake galloping could be
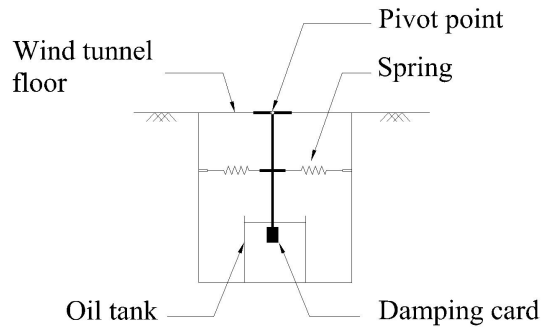95　measured.



96
97　*Figure 1: Rigid-aerodynamic-model system*

## 3. Experimental configuration

99　Wind tunnel experiments were performed in a closed-circuit wind tunnel at Yokohama National
100　University, Japan. The tunnel testing section has a width of 1.8 m and a height of 1.8 m. Figure 2
101　indicates the general configuration of the experimental test in the wind tunnel. According to the
102　research of Bearman and Morel (1983), the forces acting on the rectangular section in free stream
103　turbulence flow was lower than a smooth flow. The flow of the atmospheric boundary layer was
104　designed to simulate as a smooth flow. Figure 3 indicates the normalized wind velocity and
105　turbulence intensity which were measured by a hot-wire anemometer. The vertical direction was
106　normalized with the height of model $H_0 = 600$ mm. Also, the wind speed was normalized with the
107　reference wind velocity $U_0 = 3$ m/s at the model height. The turbulence intensity at model height was
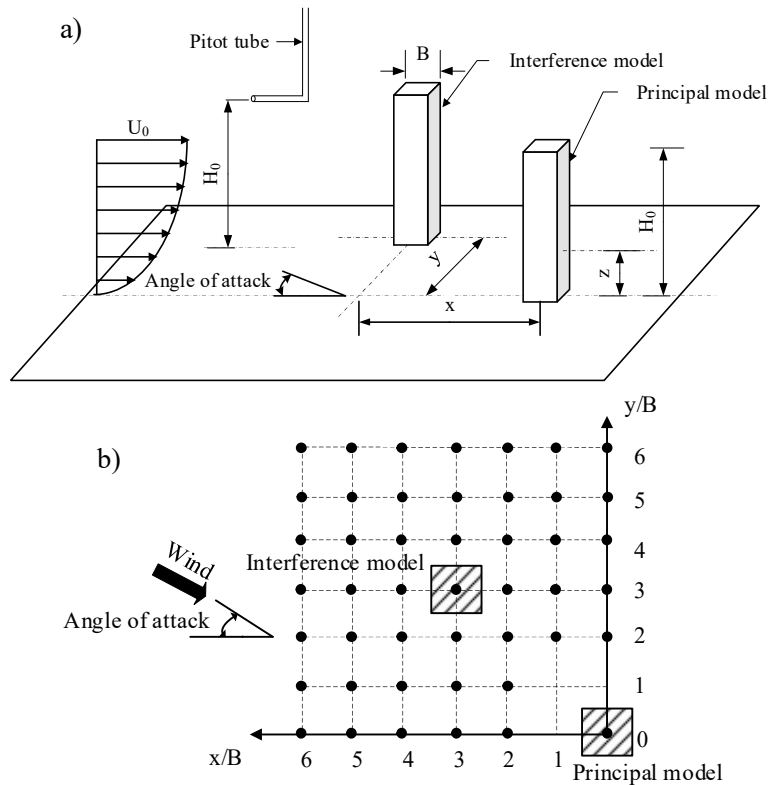108　less than 0.1 % which was considered as a smooth flow condition.



109

110
111　*Figure 2: Experiment configuration: a) Schematic of the experimental program; b) Positions of interference models*
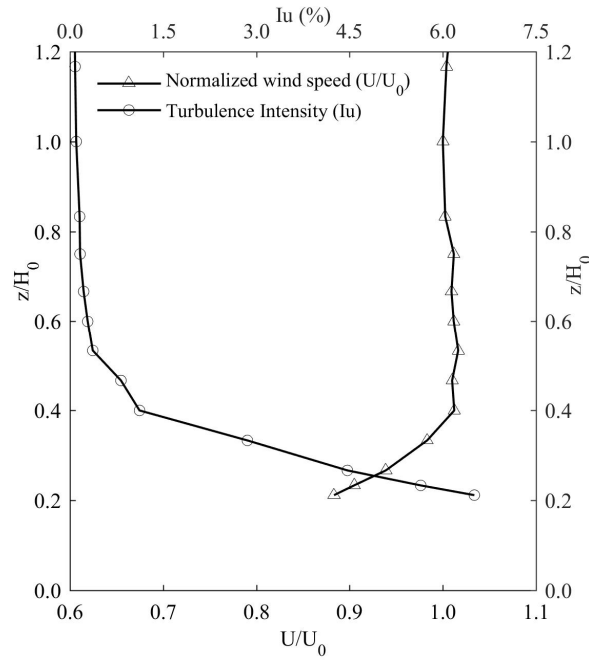
*Figure 3: Normalized wind velocity and turbulence intensity profiles*

In the static test, the velocity in the wind tunnel was calculated from the velocity in a prototype building which was estimated at 40 m/s. The velocity in the experiment at the top model height was calculated at 3 m/s by the similarity law. The Reynold number, defined by the width of the model and reference velocity, was $2.01 \times 10^4$. Ten different angles of attack were tested in different cases including 0°, 10°, 20°, 30°, 40°, 50°, 60°, 70°, 80° and 90°. An angle of 0° was represented for wind flow in the x-axis of the Cartesian coordinate. And, an angle of 90° was represented for wind flow in the y-axis of the Cartesian coordinate.
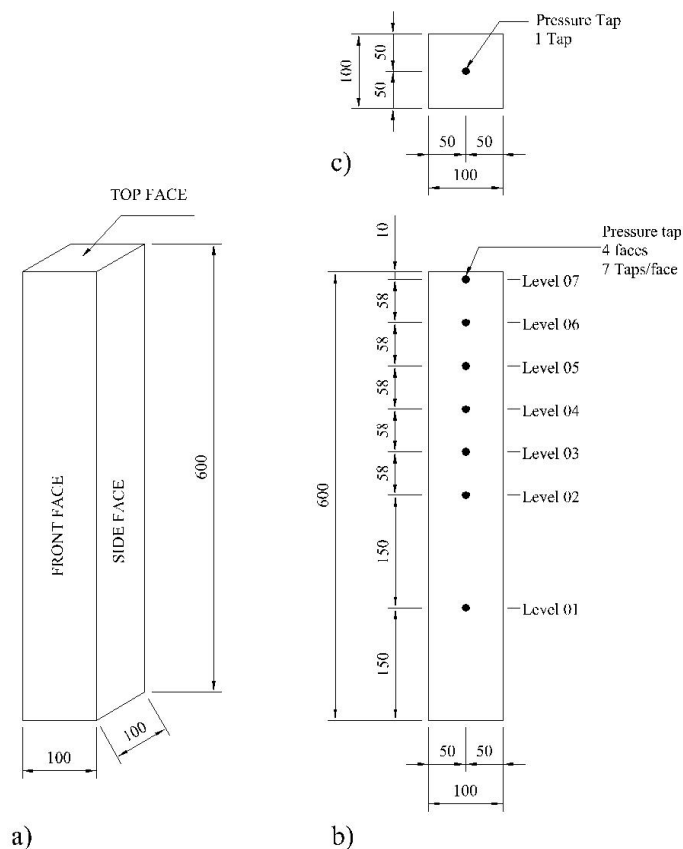
*Table 1: Previous references of reduced velocity at instability vibration*

| Reference | Testing | Model size | Reduced velocity at vortex induce vibration lock-in regime |
|---|---|---|---|
| Bailey and Kwok (1985) | Wind tunnel test: Turbulence flow, open terrain | Interference square cylinder, height:width:depth = 9:1:1 | 6 |
| Kareem (1987) | Wind tunnel test: Smooth and turbulence flow | Interference square cylinder, height:width:depth = 6:1:1 | 5-8 |
| Gowda and Kumar (2006) | Wind tunnel test | Interference circular, square, height:width:depth = 11.6:1:1 | 10-12 |
| Amandolèse and Hémon (2010) | Wind tunnel, smooth flow | Isolated square cylinder section test | 8-9 |
| Zhao (2015) | Simulation (LES), smooth flow | Rectangular cylinders with height:width = 0.3- 1.25 | 5-15 The VIV lock-in regime decreases with the increasing aspect ratio |

In the dynamic test, the wind velocity was changed at various wind speeds. Table 1 shows the previous studies which were related to this study in terms of the model dimensions and wind inflow condition. A wide range of reduced velocity at VIV lock-in regime is indicated in different tests and boundary conditions. The variation of dimensionless quantity as x/B, y/B and reduced velocity

127 $\left(U_0 \big/ f_0 B\right)$ were used in this study. To generate the lock-in regime, the reduced velocity of the isolated

128 model was from 0 to 20 which was equivalent to 0 to 10 m/s, respectively. And, reduced velocities
129 from 0 to 13 were for interference cases. More than 1190 cases of different velocities and
130 arrangements were recorded in this study.

131 The reference pressures including the total pressure and the static pressure were measured at the
132 principal model height by a pitot tube. Also, wind velocity was calculated from these data sets. The
133 total pressure of each pressure tap was synchronically measured through the acquisition system of
134 the model MT-MP-32-R1-R ±1250 Pa, MelonTechnos company in Japan, that comprised of 32
135 channels. Sampling frequency and measurement time were 200 Hz and 20 s (equivalent to 10
136 minutes for the prototype building), respectively. The mean pressure coefficient of each pressure tap
137 was calculated by $\overline{c_p} = \left(p - p_\infty\right)/q_\infty$ , where p is the total pressure at each tap, and $p_\infty$ and $q_\infty$ are the
138 reference static pressure and dynamic pressures respectively at each tap. Moreover, the displacement
139 of the principal model was measured by a laser sensor at the top of the model with the same
140 sampling frequency and measurement time to pressure measurement.



141
142 *Figure 4: Pressure tap models a) Model sizes; b) Locations of pressure taps on side faces; c) Locations of a pressure tap*
143 *on top face*

144 The design of the prototype building was in dimensions of 40×40×240 m (width × length × height),
145 the prototype building was assumed to have 60 floors with 4 m height at each story. The square
146 cross-section building models with the dimension of 0.1 m (width) × 0.1m (length) × 0.6 m (height)
147 were used in the wind tunnel test to simulate the prototype building. This model was called the
148 principal model or downstream model. The length scale was 1:400.  Pressure taps were attached to
149 the principal building model at all sides and on the top of the model. Twenty-nine pressure taps were
150 installed to investigate the pressure coefficients (Figure 4). The principal model was pivoted at the
151 base and restrained with springs in the rigid-aeroelastic-model system. Interference models were

152 wooden rigid models in the same cross-section with the principal model. One model was designed at
153 the same height of the principle model. While another was in double height. For convenience, the
154 series of interference tests with the same height interference model was denoted as group S. On the
155 other hand, group D was noted for interference tests of double height model.

156 A fundamental natural period of the prototype high-rise building was assumed as 6 s and wind speed
157 at reference height was 40 m/s. Timescale was estimated at 1:30. The expected natural frequency of
158 the model was 5 Hz. After the settlement of models, spring position and spring stiffness, the natural
159 frequency of the principal model was $f_0 = 5.00$Hz, and damping ratio was finalized at $\zeta = 1.67\%$.

160 The mean interference factor (IF) for each tap at each side was used to measure the interference
161 effect in this study. IF indicated the effect of interference model to principal model. For more details,
162 IF = 1, the mean pressure of principal model in the isolated test was the same with the pressure of
163 principal model in interference test. IF < 1, the appearance of interference model reduced the mean
164 pressure on the principal model. Finally, IF >1, the appearance of interference model increased the
165 mean pressure on the principal model. In addition, the different IF between group S and group D
166 reflected the manner of the WOT flow because group D did not generate the effect of WOT flow.
167 The IF was calculated by

168
$$\text{IF} = \frac{\text{The mean pressure coefficients for each tap in an interference test}}{\text{The mean pressure coefficients for each tap in the isolated test}}$$

169 In addition, a PIV system was installed to observe the velocity field in tandem arrangement cases for
170 group S and group D. Images of smoke particles were captured by a high-speed camera at a frame
171 rate of 1000 frames per second. These images were then analyzed by program "Flow Expert" to give
172 instantaneous flows, time-average flows, and power spectral analysis. To get high quality images, a
173 low velocity at the reference height at 2 m/s ($U_0$) was used in PIV tests.

174 **4. Validation with previous studies.**

175 To check the reliability of the wind tunnel test, the results of pressure coefficients and displacement
176 of the principal model in the isolated test and interference tests are compared to previous studies. The
177 selected works of literature are in the same flow conditions and model section test with this present
178 study: Square cylinder and smooth flow condition.

179 4.1. Validation of pressure coefficients

180 The local pressure coefficients of each side of the square cylinder in different studies are compared
181 in Table 2. Bearman and Obasaju (1982) and Nishimura and Taniike (2000) provided the distribution
182 of pressure coefficients along the cross-section of the square cylinder. The pressure coefficients of
183 each side are recalculated by deducting the value of the first measurement point. The present study
184 shows the satisfactory results to previous studies. The slight differences still can be found in the table
185 because of the differences of blockage percentages and the turbulence intensity in wind tunnel tests.
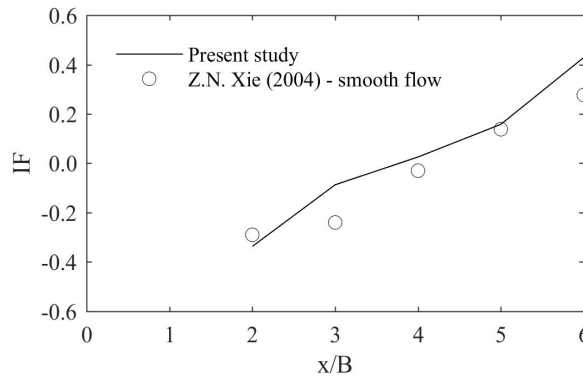186 *Table 2: Comparison of pressure coefficient of present study with previous studies*

| References | Front | Side | Rear |
|---|---|---|---|
| Bearman and Obasaju (1982) | 1.080 | -0.780 | -0.680 |
| Nishimura and Taniike (2000) | 1.000 | -0.730 | -0.615 |
| Present study | 1.086 | -0.741 | -0.668 |

187

188 4.2. Validation of interference factors

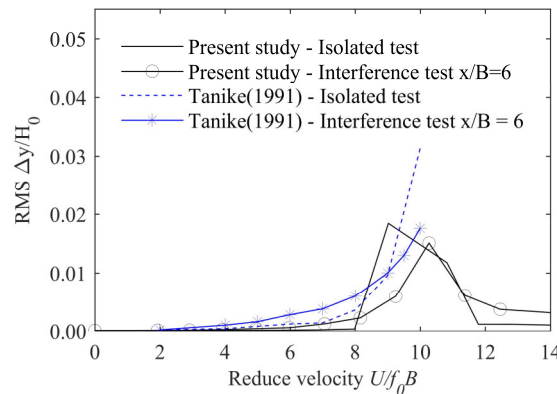189 The IFs in tandem arrangements are plotted in Figure 5 for comparison. Xie and Gu (2004)

conducted the wind tunnel test with smooth flows for square tall buildings. However, the IFs in their research were calculated based on the overturning moment in along-wind direction. The overturning moment in along-wind direction of this present study is then calculated by $OM = \sum U_0 \times \overline{c_p} \times A \times d$ where $U_0$ is reference velocity at the model height, $\overline{c_p}$ is mean pressure coefficient of each tap in the front and rear face, $A$ is the distribution area of each pressure tap, and $d$ is the distance from pressure tap to the pivot point of SDOF. Then, IFs are calculated and compared to the results of Xie and Gu (2004). The positive values of IFs show that the sign of overturning moment in interference tests are in the same sign with the isolated test. While the negative values of IFs show that the sign of overturning moment in interference tests are opposite sign with the isolated test. In the graph, differences at x/B= 3 and 6 are explained by the limitation of pressure taps on faces, which could not represent all pressure loads on the principal model. However, the trend of IF in both studies are in well agreement with each other.



*Figure 5: Validation of interference factors in tandem arrangements*

### 4.3. Validation of displacement in dynamic tests

The aerodynamic system is also validated with the results from interference effect tests of Taniike (1991). Figure 6 indicates the RMS displacement of the isolated test and the interference test of same height models (x/B = 6) in various reduce velocities. In both cases, the reduced velocity which causes the instability vibration can be seen at the same point. The difference in the mass-damping parameter as Scruton number may reflect the different behaviors in vibration. Scruton number in this study is defined as $S_c = 4\pi \dfrac{m_m}{\rho B^2} \zeta = 8.5$, where $m_m$ is the model mass ratio, $B$ is the width of the model, $\rho$ is the air density, and $\zeta$ is the damping ratio. Mannini et al. (2017) mentioned that the range of excitation due to VIV and galloping fully clarify in high Scruton number. In low Scruton number, it is difficult to distinguish clearly the velocity range which causes galloping or VIV.



*Figure 6: Comparison of single and interference case for RMS displacement in different reduced velocity*

## 5. Results and discussions

### 5.1. Mean pressure coefficient in tandem arrangements

Figure 7 shows the mean pressure coefficient $\overline{c_p}$ of pressure taps along the height of front, rear and side faces of the principal model in tandem arrangements of the isolated case, group S and group D cases. The data sets in the front face represent the trend of the WOT flow clearly. In interference tests, most of the pressure coefficients in the front face of the principal models show negative value compared to positive pressures on the front face of the isolated test. These positive pressures on the front face and negative pressures on the rear face make the drag coefficient of the whole model turn to a negative value. These results agreed well with the research of fluctuating forces on square prisms of Sakamoto et al. (1987). Moreover, the upstream models produces remarkable shielding effect on the downstream model in the along-wind direction (Xie & Gu, 2004).
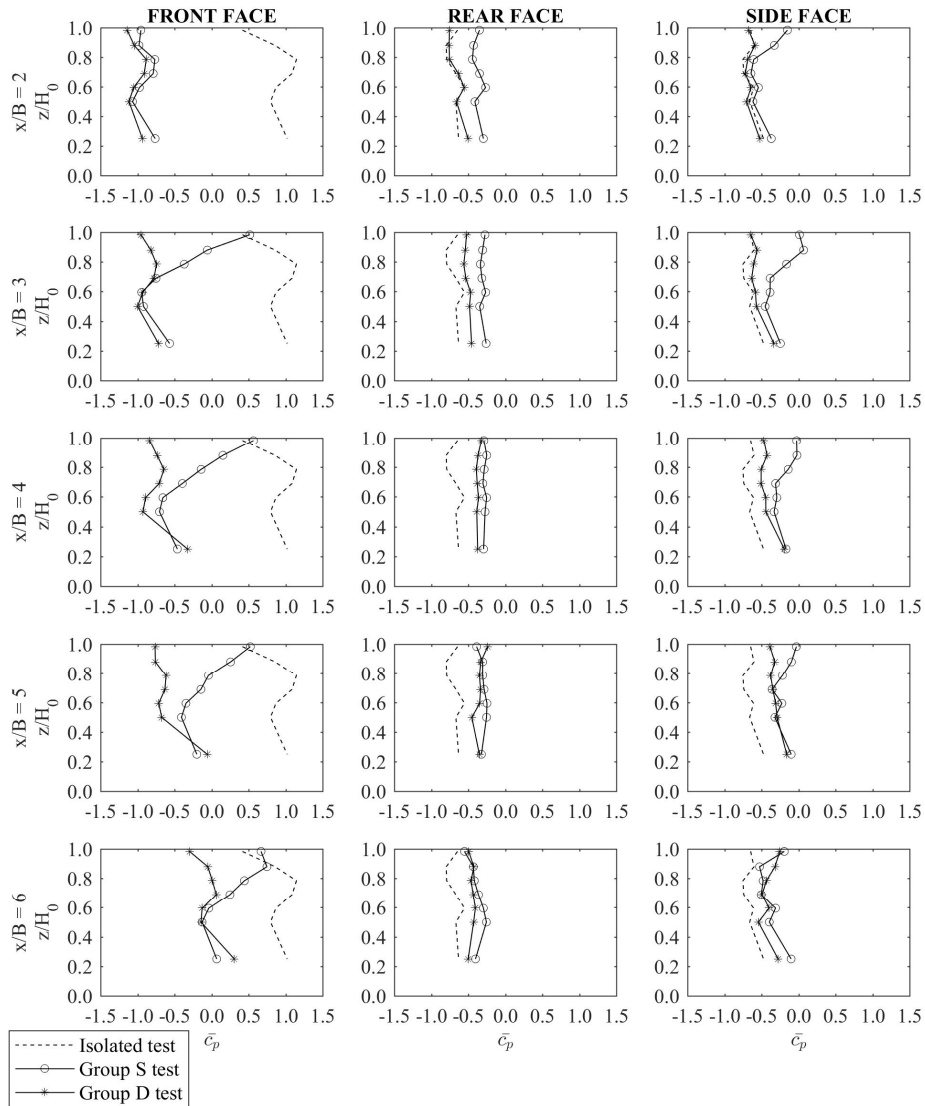


*Figure 7:Pressure coefficients on the front face of the principal model in tandem arrangements considering different interference models*

When the interference models are located near the principal model at distance of x/B = 2, no significant difference between group S and group D is observed. The WOT flow has no effect to the principal model in these cases. All positions of pressure taps indicate negative pressures. The shear layer which is formed from the separation point at top of the interference model in tests of group S

could not reach to the front face of the principal model. From x/B = 3 to 6, the pressure coefficients of the principal model in group S change gradually with respect to distance. The areas near the top turn to positive pressure area at distance x/B = 3. In this case, the shear layer from the WOT flow could move downward and reach the front face of the downstream model. When interference models in group S move further away the principal model, the area of positive pressure on the principal model increased with the increase in the distance. On the other hand, group D which is tested with double height interference model does not show this apparent trend. Pressure taps in groups S clearly prove the existence of arch-type vortex behind the flat-roof interference building as discussed by Kawai et al. (2009).

At rear and side faces, most of the cases indicate that the negative pressure in group D is lower compared to group S. Meanwhile, the rear face and side faces of the principal model in group S receive more pressure than group D due to the presence of 3-D flow combination of the WOT flow and Karman vortex. It is noted that interference models in group D only produce Karman vortex which moves downward and impacts on the sides of the principal model. This Karman vortex has no action on the rear sides at close distance as x/B = 2. Obviously, pressure coefficients in this closed arrangement indicate the same value with the isolated model case. Shifting interference models to distance x/B = 3 to 6, Karman vortex shows its effects clearly on rear and side faces. At this moment, the differences of pressure coefficients between the isolated test and group D interference test are more apparent. Therefore, Karman vortex represents its effects in the distance larger than x/B = 3 in these interference tests.
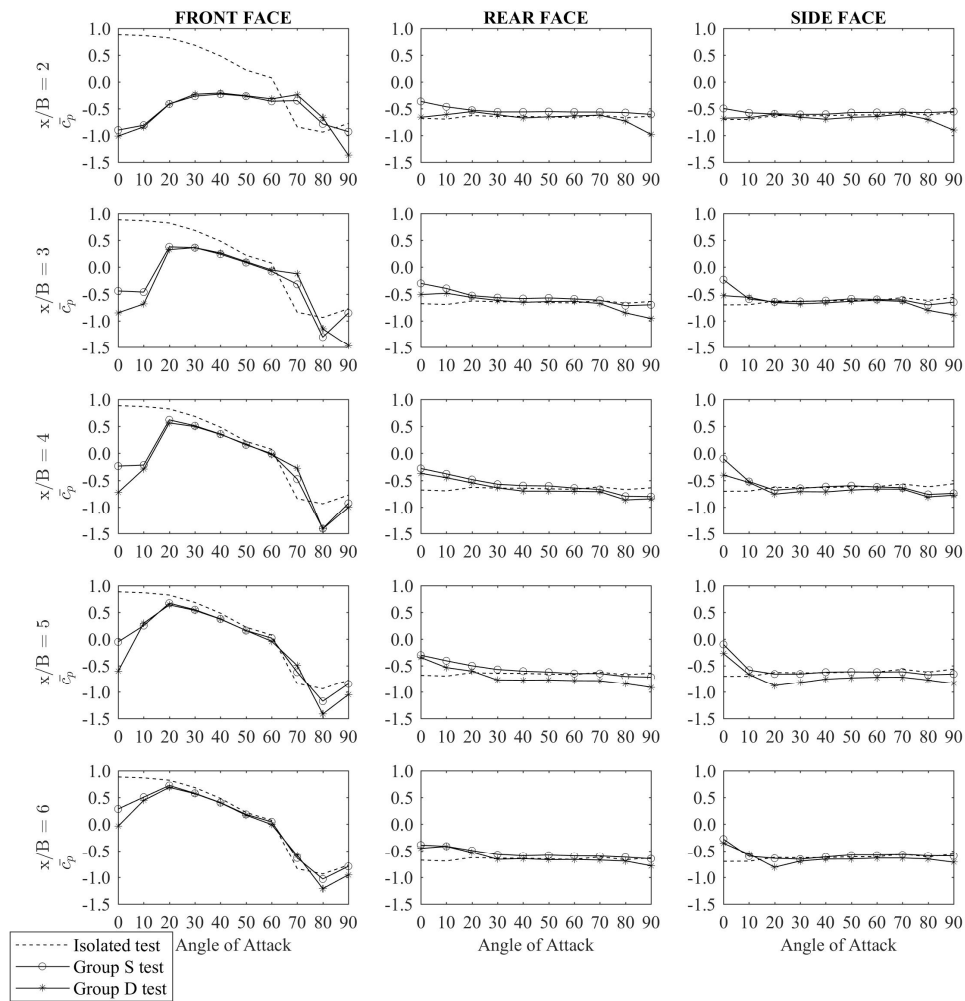


Figure 8: Mean pressure coefficients in tandem arrangements in different attack angles

256  Both the front side and rear side face of the principal model get impacts from the arch-type vortex
257  which is only generated from group S test. At the rear side, this vortex helps to reduce pressure force
258  in short distances which are less than 4B. In long distance, the arch-type vortex loses its energy to
259  contribute continuously to the pressure on the rear face. Pressure coefficients show no significant
260  difference at the rear face between group S and group D. On the other hand, the side faces are
261  interesting to observe the mixing of both Karman vortex and the WOT flow. However, the value of
262  pressure coefficients in all cases become slightly complicated to compare. Like the rear face, the
263  effects of arch-type vortex reduce when the interference models located far away from the principal
264  model. In general, the WOT flow shows its existence clearly in distance x/B = 3 to 5 in all sides.
265  These results could contribute to the building code for cladding design in the urban area and estimate
266  the dimension of the arch-type vortex.

267  The mean of pressure coefficients in different angles of attacks in tandem arrangement cases is
268  represented in Figure 8. In general, the mean of pressure coefficients of group S and group D indicate
269  a similar trend as the angle varied from 30° to 60°. The distance in across-wind direction between
270  models should be put into the consideration to explain for these results. When the angle of attack
271  becomes wider, the distance between the interference model and the principal model also increases in
272  the normal direction of wind flow. In these cases, there is a chance that the WOT flow could not
273  reach the principal model. Thus, pressure coefficients in all faces hold similar values between group
274  S and group D when the angle of attack is within 30° to 80°. However, Figure 8 indicates the gap
275  between group S and group D when the angle of attacks is 0° to 20°. It is noted that the difference
276  between tests of group S and group D is the effect of the WOT flow in contribution to the principal
277  model. Therefore, the WOT flow produces significant effects on cladding pressures of the principal
278  model for angles of attack from 0° to 20° in interference tests. Moreover, the difference of pressure
279  can be found at 90° angle of attack in the vicinity of x/B. The reason for this phenomena could be
280  explained by the channeling effect (Kim et al., 2013).
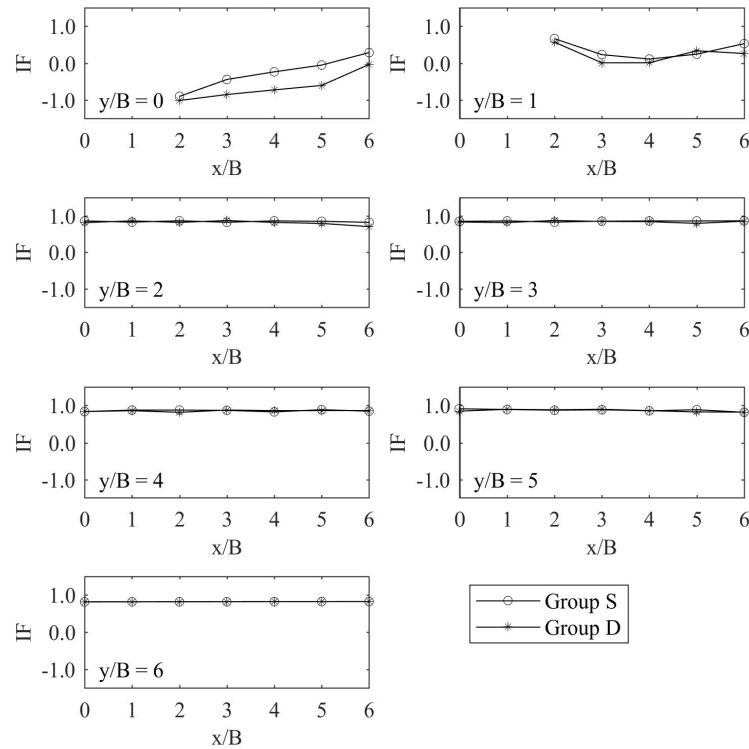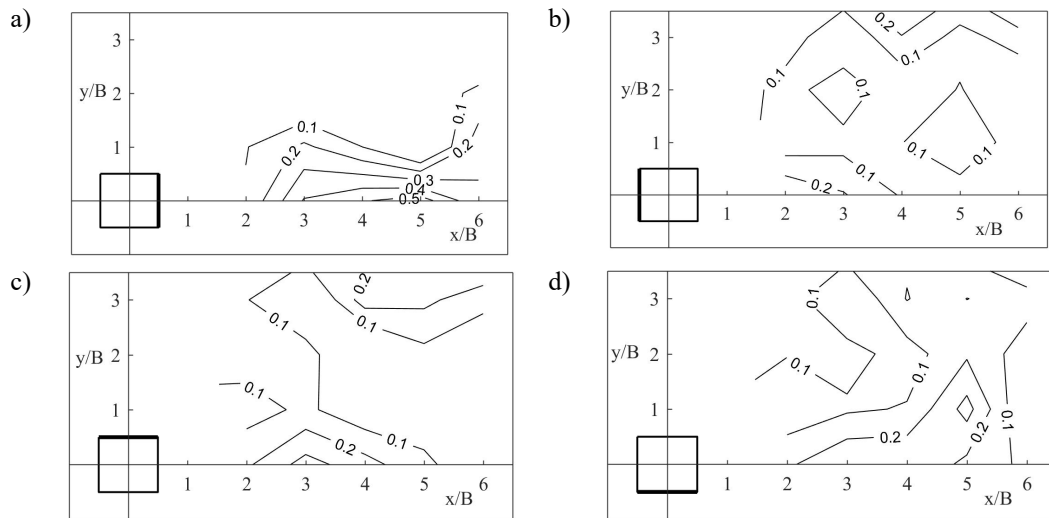
281     5.2. Interference factors



Figure 9: Mean IF of front face in the Cartesian coordinator x/B; y/B

Mean IFs on the front face in the whole domain are represented in Figure 9. It could be clearly seen in this figure the existence and contribution of the WOT flow to the principal model. The difference between two lines of group S and group D would show the effects of the WOT flow. When an interference model moves farther in the normal direction with wind flow (y/B > 2), group S and group D produce the same output of pressure on the principal model. The WOT flow has no effect to the principal model in these locations.

The major contribution can be observed in the graph of y/B = 0, 1 and 2. The WOT flow increases the pressure on the front face of the principal model. This flow is generated from the upstream interference model. After leaving the leading edge, the shear layer of the WOT flow is formed and moved downward to the principal model. The different IF between group S and group is 0.11 to 0.55 in tandem arrangement y/B = 0; 0.09 to 0.27 in stagger arrangement y/B = 1, and 0 to 0.11 in stagger arrangement y/B = 2 case. A light difference in the far distance x/B = 6 case in graph y/B =2 still can be found. There is a similar phenomenon in the previous finding when the WOT flow could have effects on the principal model within 20 ° angle of attack.

The highest difference of IF (0.55) could be observed at the position of x/B = 5 in tandem arrangement. Thus, the most contribution of the WOT flow can be found when the interference model located at x/B = 5; y/B = 0. These significant numbers would be an important addition in the cladding design of high-rise buildings to avoid the damages by wind in the urban area. At the farthest distance in tandem arrangement x/B = 6, the difference of IF between two group can still be observed. Therefore, the longer domain in along-wind direction would need to be conducted in our future research.

### 5.3. Effects of interference model's position to the WOT flow



*Figure 10: The different pressure coefficient of group S to group D:  a) Front face; b) Rear face; c) Left-side face; d) Right-side face*

As mentioned, the WOT flow is researched through the same height interference model. However, the same height interference model generates both side effects and top effects. To research the WOT flow separately, the double height interference model which only generates side effects to the principal model is also put into the concern to compare. In each position of interference models, the mean of pressure coefficients on each face is calculated. Then, the subtraction of the mean pressure coefficient in group S and mean pressure coefficient in group D is a possible value to evaluate the effect of WOT flow on each face. To have a general view of all faces, these subtraction values are represented in the form of contour lines by the linear interpolation method. Figure 10 shows the contour lines on each face. Meanwhile, these contour lines indicate the possible areas where the WOT flow could have the distribution on the principal model. The values of contour lines show how

318 much the WOT flow contribute to the mean pressure coefficient on faces. The following findings are
319 obtained from the comprehensive analysis.

320     1) The front face is the face which receives the most influence from the top flow. The strength
321        of WOT flow could contribute 46% (at position x/B = 5, y/B =0; 0.5/1.086×100) of mean
322        pressure coefficient on the front face.

323     2) The WOT flow contributes not only to the font face but also to other faces. Unlike the front
324        face, the effects from positions of interference model could not be predicted clearly.
325        However, the contribution level of WOT flow is more than 20% to the mean of face pressure
326        coefficient. Also, the effects from positions of the interference models do not indicate the
327        clear trend at the rear and side faces.

328     3) The combination of WOT flow and Karman vortex poses a considerable difficulty for
329        cladding design in high-rise buildings. The influence of WOT flow to the principal building
330        clearly cannot be neglected in all sides near the top of the model. Strengthening claddings of
331        the principal model is needed if any building is built within the affected area which is shown
332        in Figure 10. Moreover, the design of the roof needs to consider the aerodynamic shape to
333        avoid or reduce the pressure from the shear layer of WOT flow.

334     5.4. Dynamic tests

335 VIV is investigated in the across-wind direction in various reduce velocities. The top displacement of
336 the principal model is recorded in the isolated case and interference cases. Figure 11 represents the
337 RMS displacement in the form of a dimensionless unit by dividing the RMS displacement by the
338 height of the principal model. In most cases, the interference tests reduce the amplitude of vibration
339 on the principal model compared to the isolated test. These reductions are explained by the shielding
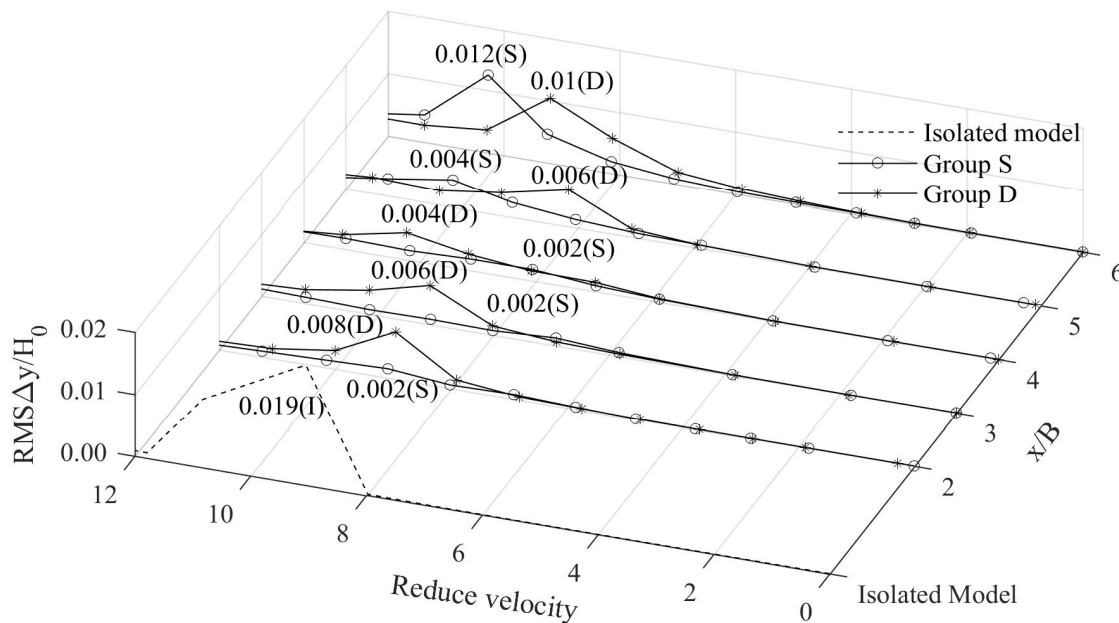340 effect. Two important results could be obtained as follows.



341
342 *Figure 11: RMS displacement in various reduce velocities in tandem arrangements: (I): Isolated model; (S): Group S;*
343 *(D): Group D*

344     1) When two models in group S are in distance x/B ≤ 4 in the tandem arrangement, the VIV still
345        occurs but with very small amplitude of vibration. The amplitude of VIV in these cases is not
346        much different with the amplitude in adjacent velocity. On the other hand, group D shows the
347        clear peak of the amplitude in VIV. The reason could be explained that the interference

348 model in group D produces the Karman vortex which causes the vibration of the downstream
349 model. While the Karman vortex in group S is mixed with the WOT flow so that the effect of
350 Karman vortex on the downstream model is reduced.

351 2) In farther distance, x/B>4, the VIV in group S occurs in higher velocity than group D.
352 Moreover, the amplitude at VIV of group S increases significantly. The oscillation is more
353 pronounced when interference models are at the distance x/B = 6. At x/B = 5 and x/B =6, the
354 appearance of the WOT flow properly makes the principal model vibrate at higher reduced
355 velocity. Meanwhile, the building can resist larger velocity before turning to instability
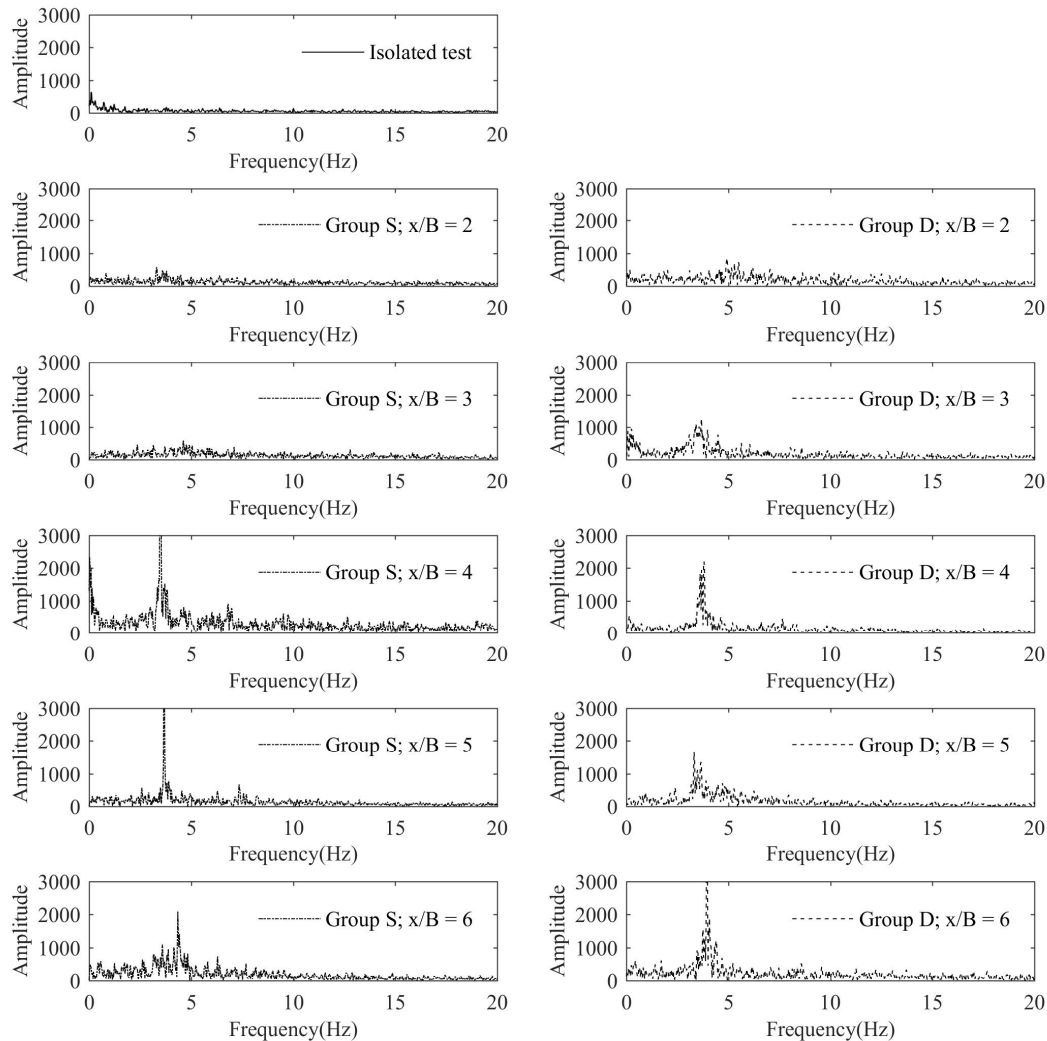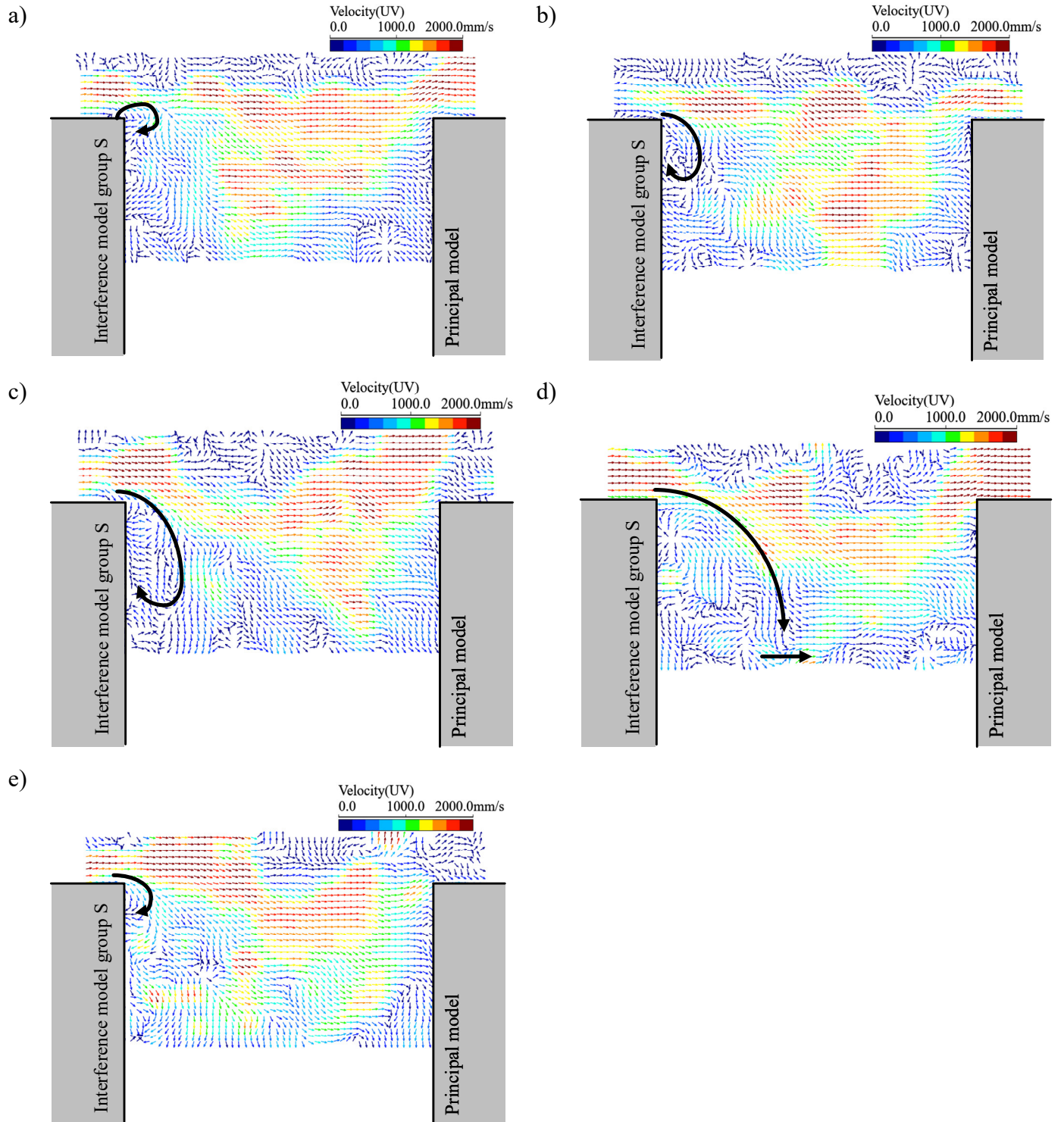356 vibration on the site.



357
358 *Figure 12: Fast Fourier Transform (FFT) of wake fluctuation on the side face of the principal model in tandem*
359 *arrangements*

360 The analysis of power spectrum on the side of the principal model (Figure 12) explains more clearly

361 for VIV and Strouhal number $St = \dfrac{fB}{U_0}$ where $f$ is the frequency of vortex shedding. In close

362 distances, the peak amplitude is not clear enough to distinguish from other adjacent points according
363 to the slight vibration in VIV for all cases. Whereas, from x/B = 3 in group S and group D, the peak
364 is extremely sharped. The frequency at the peak in each case increases with the increase of the
365 distance between two models in interference tests. The amplitude of group S in x/B = 4 and 5 is
366 lower than group D, while the opposite phenomenon is observed in distance x/B = 6. The critical
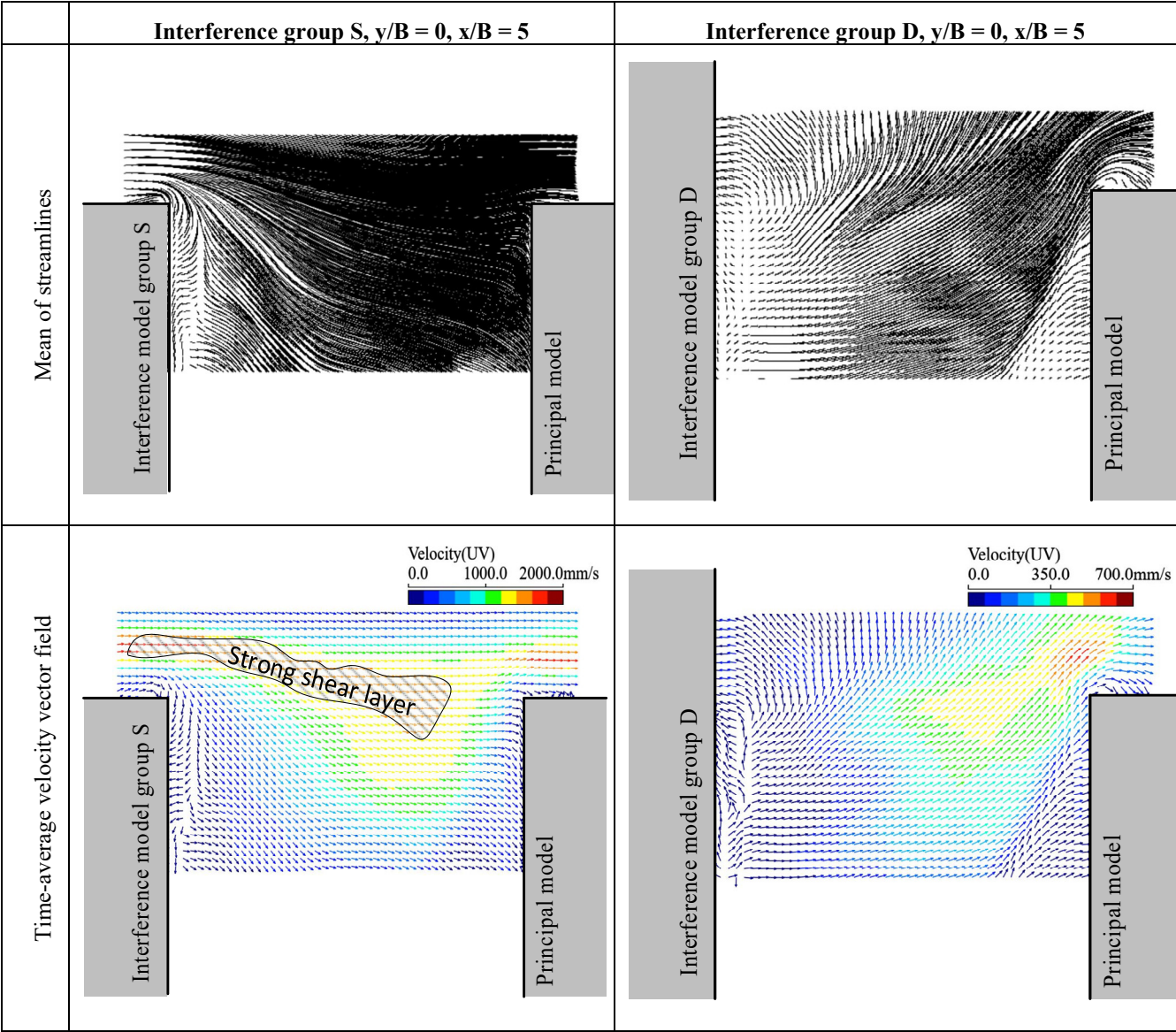367 position for interference model may be located in between x/B = 5 and x/B = 6. Moreover, Strouhal

numbers are calculated from these peaks of power spectrum graphs. This number is directly proportional to the frequency of the vortex shedding. The distance between the two models in interference tests is farther, the higher Strouhal number is obtained. These results are in agreement with those from Sakamoto et al. (1987).

## 5.5. PIV images



Figure 13: Instantaneous images of velocity field in group S, x/B = 5, y/B = 0: a) T = 0/4; b) T = 1/4; c) T = 2/4; d) T = 3/4; e) T = 4/4;

376     An example of flow visualization in tandem arrangement group S at x/B = 5 is shown in Figure 13.
377     Five instantaneous images are selected to represent the flow in one period of vortex shedding (T)
378     which can be calculated from the frequency of vortex shedding in Figure 12 (Group S; x/B =5: $f$ =
379     3.687 Hz). The vortex is always present under the shear layer of the WOT flow which is generated
380     from the top of the upstream model and developed to downstream. Due to this vortex, the area on the
381     leeward side of the interference model is in negative pressures. Figure 13a shows the vortex which is
382     initially generated on the leading edge at top of the interference model. Then, the size of the vortex
383     keeps increasing between the streamwise and downward direction (Figure 13b, c). These vortices are
384     in different sizes in different times but always start from the edge of the flat roof. However, this kind
385     of vortex is easy to lose its energy when moving down and mixes up with the side flow which is
386     generated from the lower wall on the vertical edges of the upstream model (Figure 13d). In these
387     figures, the shear layer of the WOT flow tend to move downward after leaving the roof of the
388     interference model.

389



390     *Figure 14: Mean streamlines and time-average velocity vector field at x/B = 5; y/B = 0*

391     Figure 14 shows the mean of streamlines and time-average velocity vector fields of tandem
392     arrangements at distance of x/B = 5. A part of models is also represented in this figure. These images

are obtained by averaging all instantaneous images. The analysis of mean of streamlines and time-average velocity vector fields gives an overall image of WOT flow regardless of time.

In streamline results, the shear layer of WOT flow passes the roof, tends to go down and heads to the front side of the principal model. With this shear layer, the areas near the top of the principal model turn into positive pressure area and even receive more pressure than the isolated test. The same results are shown in Figure 7 when showing the high-pressure value on the pressure near the top of the principal model. On the other hand, group D without WOT flow does not form the shear layer behind the leeward wall of the interference model. The low pressures between two models and the presence of Karman vortex make all sides of the principal model turn to negative pressures at all positions.

In time-average velocity vector fields results, the shear layer of WOT flow generated on the flat roof of the interference model group S moves downward and downs to lower level of the principal model. The magnitude vector inside of shear layer of WOT flow slightly decreases along the wind flow direction. This means that the pressure could also reduce if the distance between two models increases. Thus, the most affected areas are the one near the top of the principal model, while the lower areas along the height of model suffer less effect.

## 6. Conclusions

In this study, the WOT flow in square cylinder high-rise buildings are investigated and systematically studied through a series of static and dynamic wind tunnel tests. The contribution of WOT flow in different locations is analyzed, and following conclusion can be inferred:

1) The WOT flow has strong effects in the same height models. At position x/B = 5, y/B =0 of the same height upstream model, the WOT flow could contribute 46% of pressure coefficient to the front face of the principal model. Even though there is a model in the upstream direction and it presents as the shielding model, a part of the front face of the principal model shows higher positive pressures compared to the isolated test. When the distance between the upstream model and the downstream model is lengthened, the affected area on the front face increases because of shear layer generated from WOT flow.

2) In dynamic vibration, the presence of the WOT flow in interference tests makes the principal model vibrate in small amplitude within the distance x/B = 2 to 4 in tandem arrangement. In farther distance (x/B = 5, 6), the contribution of the WOT flow in group S make VIV occur in a higher reduced velocity compared to both isolated tests and group D. Meanwhile, in all distances of tandem arrangement, the WOT flow provides the beneficial effects in terms of dynamic structural designs. Therefore, buildings on the site can resist better by the contribution of the WOT flow.

## 7. Acknowledgements

## 8. References

Amandolèse, X., & Hémon, P. (2010). Vortex-induced vibration of a square cylinder in wind tunnel. *Comptes Rendus Mécanique, 338*(1), 12-17. doi:https://doi.org/10.1016/j.crme.2009.12.001

Bailey, P. A., & Kwok, K. C. S. (1985). Interference excitation of twin tall buildings. *Journal of Wind Engineering and Industrial Aerodynamics, 21*(3), 323-338. doi:http://dx.doi.org/10.1016/0167-6105(85)90043-1

Balendra, T., & Nathan, G. (1987). Longitudinal, lateral and torsional oscillations of a square section tower model in an atmospheric boundary layer. *Engineering Structures, 9*(4), 218-224.

Banks, D., & Meroney, R. N. (2001a). The applicability of quasi-steady theory to pressure statistics beneath roof-top vortices. *Journal of Wind Engineering and Industrial Aerodynamics, 89*(6), 569-598.

439         doi:https://doi.org/10.1016/S0167-6105(00)00092-1

440 Banks, D., & Meroney, R. N. (2001b). A model of roof-top surface pressures produced by conical vortices: Model
441         development. *Wind and Structures, 4*(3), 227-246.

442 Banks, D., Meroney, R. N., Sarkar, P. P., Zhao, Z., & Wu, F. (2000). Flow visualization of conical vortices on flat roofs
443         with simultaneous surface pressure measurement. *Journal of Wind Engineering and Industrial Aerodynamics,*
444         *84*(1), 65-85. doi:https://doi.org/10.1016/S0167-6105(99)00044-6

445 Bearman, P. W., & Morel, T. (1983). Effect of free stream turbulence on the flow around bluff bodies. *Progress in*
446         *Aerospace Sciences, 20*(2), 97-123. doi:https://doi.org/10.1016/0376-0421(83)90002-7

447 Bearman, P. W., & Obasaju, E. D. (1982). An experimental study of pressure fluctuations on fixed and oscillating
448         square-section cylinders. *Journal of fluid mechanics, 119*, 297-321. doi:10.1017/S0022112082001360

449 Gowda, B. H. L., & Kumar, R. (2006). Flow-induced oscillations of a square cylinder due to interference effects. *Journal*
450         *of sound and vibration, 297*(3), 842-864. doi:http://dx.doi.org/10.1016/j.jsv.2006.05.003

451 Hui, Y., Tamura, Y., & Yoshida, A. (2012). Mutual interference effects between two high-rise building models with
452         different shapes on local peak pressure coefficients. *Journal of Wind Engineering and Industrial Aerodynamics,*
453         *104–106*, 98-108. doi:http://dx.doi.org/10.1016/j.jweia.2012.04.004

454 Kareem, A. (1987). The effect of aerodynamic interference on the dynamic response of prismatic structures. *Journal of*
455         *Wind Engineering and Industrial Aerodynamics, 25*(3), 365-372.

456 Kawai, H. (2002). Local peak pressure and conical vortex on building. *Journal of Wind Engineering and Industrial*
457         *Aerodynamics, 90*(4–5), 251-263. doi:http://dx.doi.org/10.1016/S0167-6105(01)00218-5

458 Kawai, H., Okuda, Y., & Ohashi, M. (2009). *Three dimensional structures of flow behind a square prism.* Paper
459         presented at the The Seventh Asia-Pacific Conference on Wind Engineering.

460 Kawai, H., Okuda, Y., & Ohashi, M. (2012). Near wake structure behind a 3D square prism with the aspect ratio of 2.7 in
461         a shallow boundary layer flow. *Journal of Wind Engineering and Industrial Aerodynamics, 104*, 196-202.

462 Kim, W., Tamura, Y., & Yoshida, A. (2009). *Interference effects of two buildings on peak wind pressures.* Paper
463         presented at the The Seventh Asia-Pacific Conference on Wind Engineering.

464 Kim, W., Tamura, Y., & Yoshida, A. (2013). Simultaneous Measurement of Wind Pressures and Flow Patterns for
465         Buildings with Interference Effect. *Advances in Structural Engineering, 16*(2), 287-305. doi:10.1260/1369-
466         4332.16.2.287

467 Kim, W., Tamura, Y., & Yoshida, A. (2015). Interference effects on aerodynamic wind forces between two buildings.
468         *Journal of Wind Engineering and Industrial Aerodynamics, 147*, 186-201.
469         doi:http://dx.doi.org/10.1016/j.jweia.2015.10.009

470 Mannini, C., Marra, A. M., Massai, T., & Bartoli, G. (2017). *Low-speed galloping for rectangular cylinders with side*
471         *ratios larger than unity.* Paper presented at the title JAXA Special Publication: Proceedings of the First
472         International Symposium on Flutter and its Application 宇宙航空研究開発機構特別資料.

473 Marwood, R., & Wood, C. J. (1997). Conical vortex movement and its effect on roof pressures. *Journal of Wind*
474         *Engineering and Industrial Aerodynamics, 69-71*, 589-595. doi:https://doi.org/10.1016/S0167-6105(97)00189-X

475 Nishimura, H., & Taniike, Y. (2000). Fluctuating pressures on a two-dimensional square prism. *Journal of Structural and*
476         *Construction Engineering*(533), 37-43.

477 Pindado, S., Meseguer, J., & Franchini, S. (2011). Influence of an upstream building on the wind-induced mean suction
478         on the flat roof of a low-rise building. *Journal of Wind Engineering and Industrial Aerodynamics, 99*(8), 889-
479         893.

480 Sakamoto, H., Hainu, H., & Obata, Y. (1987). Fluctuating forces acting on two square prisms in a tandem arrangement.
481         *Journal of Wind Engineering and Industrial Aerodynamics, 26*(1), 85-103. doi:http://dx.doi.org/10.1016/0167-
482         6105(87)90037-7

483 Taniike, Y. (1991). Turbulence effect on mutual interference of tall buildings. *Journal of engineering mechanics, 117*(3),
484         443-456.

485 Taniike, Y. (1992). Interference mechanism for enhanced wind forces on neighboring tall buildings. *Journal of Wind*
486         *Engineering and Industrial Aerodynamics, 42*(1-3), 1073-1083. doi:10.1016/0167-6105(92)90114-p

487 Thanh, T. N., Yamada, H., & Katsuchi, H. (2005). *Motion-dependent forces in high-rise building.* Paper presented at the

488    2005 Structures Congress and the 2005 Forensic Engineering Symposium-Metropolis and Beyond.

489    Wu, F., Sarkar, P. P., Mehta, K. C., & Zhao, Z. (2001). Influence of incident wind turbulence on pressure fluctuations
490        near flat-roof corners. *Journal of Wind Engineering and Industrial Aerodynamics, 89*(5), 403-420.
491        doi:https://doi.org/10.1016/S0167-6105(00)00072-6

492    Xie, Z. N., & Gu, M. (2004). Mean interference effects among tall buildings. *Engineering Structures, 26*(9), 1173-1183.
493        doi:http://dx.doi.org/10.1016/j.engstruct.2004.03.007

494    Yahyai, M., Kumar, K., Krishna, P., & Pande, P. (1992). Aerodynamic interference in tall rectangular buildings. *Journal
495        of Wind Engineering and Industrial Aerodynamics, 41*(1-3), 859-866.

496    Yan, B. W., & Li, Q. S. (2016). Wind tunnel study of interference effects between twin super-tall buildings with
497        aerodynamic modifications. *Journal of Wind Engineering and Industrial Aerodynamics, 156*, 129-145.
498        doi:http://dx.doi.org/10.1016/j.jweia.2016.08.001

499    Yoshie, R., Kawai, H., Shimura, M., & Wei, R. (1997). A study on wind-induced vibration of super high rise building by
500        multi-degree-of freedom model. *Journal of Wind Engineering and Industrial Aerodynamics, 69*, 745-755.
501        doi:http://dx.doi.org/10.1016/S0167-6105(97)00202-X

502    Yu, X. F., & Xie, Z. N. (2015). *Interference effects on wind pressure distribution for high-rise buildings*. Paper presented
503        at the The 14th International Conference on Wind Engineering ICWE14, Porto Alegre - Brazil.

504    Zdravkovich, M. (1985). Flow induced oscillations of two interfering circular cylinders. *Journal of sound and vibration,
505        101*(4), 511-521.

506    Zhao, M. (2015). Flow-induced vibrations of square and rectangular cylinders at low Reynolds number. *Fluid Dynamics
507        Research, 47*(2), 025502.

508